

Conversion of CO₂ to higher alcohols on K-CuZnAl/Zr-CuFe composite

Qian Zhang^{a,b}, Sen Wang^{a,*}, Xuerong Shi^{c,*}, Mei Dong^a, Jiangang Chen^a, Juan Zhang^a,
Jianguo Wang^{a,b}, Weibin Fan^{a,*}

^a State Key Laboratory of Coal Conversion, Institute of Coal Chemistry, Chinese Academy of Sciences, P.O. Box 165, Taiyuan, Shanxi 030001, PR China

^b University of the Chinese Academy of Sciences, Beijing 100049, PR China

^c School of Materials Science and Engineering, Shanghai University of Engineering Science, Shanghai 201620, PR China

ARTICLE INFO

Keywords:

CO₂ hydrogenation

Higher alcohols

CuFeO_x

Zr dopant

Composite catalyst

ABSTRACT

Direct conversion of CO₂ into higher alcohols (C₂₊OH) is highly desirable, but rather challenging due to requiring the synergetic action of C-C coupling and CO insertion. Here, we developed a new K-CuZnAl/Zr-CuFe composite, which gave CO₂ conversion and C₂₊OH selectivity of 40.6% and 22.4% respectively, while CO selectivity is only 10.3% at 320 °C, 4 MPa and 6000 mL g_{cat}⁻¹ h⁻¹. The C₂₊OH STY can reach 195.1 mg g_{cat}⁻¹ h⁻¹, and is well maintained within 200 h at higher GHSV of 24000 mL g_{cat}⁻¹ h⁻¹. Introduction of K-CuZnAl and decrease of the contact distance of K-CuZnAl and Zr-CuFe boost the formation and subsequent conversion of CO* intermediate. In addition, doping small amounts of Zr into CuFe catalyst hinders the phase separation of Cu and Fe species by enhancing their interface interaction. As a result, the CH_x* species generated on iron carbide through CO* dissociative activation quickly reacts with the non-dissociative adsorbed CO* on adjacent Cu to produce more C₂₊OH.

1. Introduction

Massive consumption of fossil fuels causes large amounts of CO₂ emission which is considered to cause a serious global greenhouse effect. However, on the other hand, CO₂ is a non-toxic and abundant carbon source [1,2]. By catalytic hydrogenation, it can be converted into light olefins, aromatics, liquefied petroleum gas (LPG), gasolines, etc [3–9]. This can not only effectively mitigate the CO₂ emission amount and alleviate the greenhouse effect, but also open up new ways to synthesize value-added chemicals.

Alcohols are important solvents, additives or essential building-block molecules for synthesis of esters, detergents and surfactants [10,11]. Nowadays, conversion of CO₂ into methanol has been industrialized. The mostly used catalysts are modified copper-zinc-aluminum (CuZnAl), although indium oxide (In₂O₃), zinc-zirconium solid solution (ZnZrO_x) and molybdenum sulfide (MoS₂) have been developed [12–15]. Compared with methanol, C₂₊ higher alcohols (C₂₊OH) with higher energy density are more difficult to be synthesized, due to requirement of synergetic execution of C-C coupling and CO insertion [16].

Pt, Pd, Rh or Ir-based noble metal catalysts have been proved to show excellent performance in CO₂ hydrogenation to C₂₊OH [17–19]. Wang and co-workers reported that Na-Rh embedded in silicalite-1 catalyst

(Na-Rh@S-1) exhibited C₂₊OH selectivity and space time yield (STY) of ~30% (ethanol accounting for 80% of C₂₊OH) and 0.49 mmol g_{cat}⁻¹ h⁻¹ at CO₂ conversion of 10% [20]. The space confinement effect of silicalite-1 endows high catalytic stability with the catalytic life of 100 h. By optimizing Pt loading and reaction conditions, ordered Pt/Co₃O₄ sample gave the ethanol selectivity and STY of 82.0% and 0.51 mmol g_{cat}⁻¹ h⁻¹ [21]. Recently, a more interesting single-atom catalyst of Ir-In₂O₃ was developed by Ye and co-workers. This catalyst showed the ethanol selectivity and STY as high as 99% and 0.99 mmol g_{cat}⁻¹ h⁻¹ [22], as the isolated Ir atom anchored on the oxygen vacancies of In₂O₃ formed Lewis acid-base pair, which not only promotes activation of CO₂ to CO*, but also accelerates the C-C coupling between CO* and methoxy group. Regardless of the good catalytic results of these noble metal-based samples, their high prices limit the large-scale industrial applications.

Thus, design of CuFe-based catalysts has attracted great interest due to their good performance and low price [23]. Liu et al. found that Cs-CuFeZn catalyst was a potential candidate for the formation of higher alcohols, with the selectivity and STY of 19.8% and 73.4 mg g_{cat}⁻¹ h⁻¹, along with CO₂ conversion of 36.6%, at 330 °C and 5.0 MPa [24]. The selectivity of C₂₊OH can be further elevated to 22.8% on K-CuZnMgFe catalyst, despite that its STY is slightly decreased to 69.6 mg g_{cat}⁻¹ h⁻¹ due to the decline of CO₂ conversion [25]. For CuFe-based catalysts, it is

* Corresponding authors.

E-mail addresses: wangsen@sxicc.ac.cn (S. Wang), shixuer05@mails.ucas.ac.cn (X. Shi), fanwb@sxicc.ac.cn (W. Fan).

<https://doi.org/10.1016/j.apcatb.2024.123748>

Received 7 November 2023; Received in revised form 10 January 2024; Accepted 15 January 2024

Available online 18 January 2024

0926-3373/© 2024 Elsevier B.V. All rights reserved.

considered that CO* is firstly generated from reverse water-gas shift (RWGS) reaction on Cu sites, and then, is transformed into CH_x* on iron carbide (e.g. Fe₅C₂) and further into C_xH_y species through CH_x*-CH_x* coupling, or interacted with the non-dissociative CO* adsorbed on the adjacent Cu site to form higher alcohols through the insertion and subsequent acyl hydrogenation [26].

It has been shown that CuFe catalyst produces large amounts of hydrocarbons because of significant CH_x*-CH_x* coupling, and introduction of alkali metal into CuZnAl generates more non-dissociated CO* species. Thus, coupling of the alkali metal, e.g. potassium, -modified CuZnAl and the CuFe catalyst would enhance the reaction of CO* with CH_x* and produce more higher alcohols [27]. Recently, Liu and co-workers prepared CuZnAl/K-CuMgZnFe composite, which gave higher CO₂ conversion (42.3%) and C₂₊OH STY (around 106 mg g_{cat}⁻¹ h⁻¹) than sole K-CuMgZnFe (30.4% and 70.6 mg g_{cat}⁻¹ h⁻¹) in CO₂ hydrogenation [28]. Nevertheless, the selectivity of higher alcohols is still only 17.4%. These researches show that although CO₂ hydrogenation to C₂₊OH has been made significant progress, the C₂₊OH selectivity and STY are unsatisfactory yet. Therefore, development of a highly efficient catalyst system for hydrogenation of CO₂ to higher alcohols is still a challenge.

Here, a new K-CuZnAl/Zr-CuFe composite was designed, and it gave CO₂ conversion and C₂₊OH selectivity of 40.6% and 22.4% respectively but CO selectivity of only 10.3% at 320 °C, 4 MPa and 6000 mL g_{cat}⁻¹ h⁻¹. When the GHSV was increased to 24000 mL g_{cat}⁻¹ h⁻¹, the C₂₊OH STY reached 195.1 mg g_{cat}⁻¹ h⁻¹. The Rietveld refined XRD, XPS, Aberration-corrected HAADF-STEM and EDX elemental mapping, CO/CO₂-TPD, H₂-TPR, XANES/EXAFS, in situ DRIFTS, PTR TOF MS and DFT calculation results indicate that introduction of K-CuZnAl and regulation of the contact distance of K-CuZnAl and Zr-CuFe can generate more non-dissociative CO* species, and addition of small amounts of Zr into CuFe sample enhances the interaction of Cu with Fe, which allows CH_x* formed on iron carbide site to rapidly interact with the non-dissociative CO* adsorbed on adjacent Cu site. Therefore, the formation of C₂₊OH is significantly promoted.

2. Experimental section

2.1. Catalyst preparation

The commercial Cu/ZnO/Al₂O₃ was kindly provided by Sinopec Nanhua Group Research Institute. K-modified Cu/ZnO/Al₂O₃ was prepared by incipient wetness impregnation method. Designed amounts of potassium nitrate (KNO₃) was firstly dissolved in 5 mL deionized water. Then, the obtained solution was dropwise added into CuZnAl catalyst. The resultant mixture was subsequently sonicated for 30 min and dried at 100 °C overnight. The obtained solid with a K loading ~4 wt% was finally calcined at 550 °C for 4 h.

A series of Zr(x)-CuFe oxides with different Zr contents were fabricated by the co-precipitation (CP) method. Certain amounts of copper nitrate (Cu(NO₃)₂•3 H₂O), iron nitrate (Fe(NO₃)₃•9 H₂O) and/or zirconium nitrate (Zr(NO₃)₄•5 H₂O) were dissolved in deionized water to obtain solution I with the concentration of total metal ions of 0.3 M. Solution II was prepared by dissolving a certain amount of potassium hydroxide (KOH) in deionized water with a concentration of 1.14 M. Then, the solution I was slowly added into the solution II at stirring condition by keeping pH value at 10.0. After being aged at 70 °C for 3 h, the obtained precipitate was filtrated and washed with water several times. The solid sample was dried at 100 °C for 8 h and calcined at 450 °C for 4 h. The residual potassium content in the solid samples was controlled to around 1.2–1.5 wt% by adjusting washing times. The resultant solid was designed as Zr(x)-CuFe with x representing the Zr/Cu molar ratio. Unless otherwise specified, the Cu/Fe molar ratio was 1.

KCuZnAl/Zr(x)-CuFe composites were fabricated by uniformly mixing the powders of the two components with a weight ratio of 1/1. They were pressed and crushed into 20–40 mesh particles. For comparison,

KCuZnAl/Zr(x)-CuFe composites were also prepared by granule stacking method, where the 20–40 mesh KCuZnAl and Zr(x)-CuFe particles were homogeneously mixed with weight ratio of 1/1.

2.2. Catalyst Characterization

The crystal structure, texture properties, morphology, and catalytic mechanism of various Zr(x)-CuFe samples were investigated by powder X-ray diffraction (PXRD), high-resolution Transmission electron microscopy (HRTEM), X-ray photoelectron spectra (XPS), N₂ sorption experiment, temperature-programmed reduction of H₂ (H₂-TPR), temperature-programmed desorption of CO₂/CO (CO₂-TPD or CO-TPD), in situ diffuse reflectance infrared Fourier transform spectroscopy (DRIFTS), temperature programmed surface reaction of CO hydrogenation (CO-TPSR) with proton transfer reaction time of flight mass (PTR TOF-MS) spectrometry and Density Functional Theory (DFT) calculation.

2.3. Catalytic evaluation

The catalytic evaluation for hydrogenation of CO₂ to higher alcohols was conducted in a fixed-bed reactor with 10 nm inner diameter (I.D.). 0.4 g composite sample was placed in the middle of reactor. The samples were pre-reduced at 400 °C for 2 h in a pure H₂ flow of 30 mL min⁻¹. When the reaction temperature was lowered to 300 °C, H₂ and CO₂ mixture (H₂/CO₂ = 3/1) was fed into the reactor. The CO₂ hydrogenation was carried out at 300 °C, 4.0 MPa and GHSV of 6000 mL g⁻¹/h unless otherwise specified.

The reaction products were on-line detected with an Agilent 7890 A gas chromatograph (GC) equipped with one thermal conduction detector (TCD), two flame ionization detectors (FIDs) and two capillary columns (J&W 127–7031, 30 m × 530 μm × 0.25 μm; Agilent 19095 P-S25, 50 m × 530 μm × 15 μm). The pipeline between reactor and GC were maintained at 100 °C to avoid product condensation. The CO₂ conversion (x(CO₂)) and the CO selectivity (s(CO)) were evaluated by following equations:

$$x(\text{CO}_2) = \frac{n(\text{CO}_2, \text{in}) - n(\text{CO}_2, \text{out})}{n(\text{CO}_2, \text{in})} \times 100\%$$

$$s(\text{CO}) = \frac{n(\text{CO}, \text{out})}{n(\text{CO}_2, \text{in}) - n(\text{CO}_2, \text{out})} \times 100\%$$

where n(CO₂,in) is the CO₂ amount introduced into the reactor, and n(CO₂,out) and n(CO,out) are the amounts of CO₂ and CO discharged in the effluents respectively. The alcohols (C_iOH) and hydrocarbons (C_iH_{jx}) selectivity (CO free) were calculated by the following equations [29,30],

$$s(\text{C}_i\text{OH}) = \frac{n(\text{C}_i\text{OH})}{\sum i \bullet n(\text{C}_i\text{H}_{jx}) + n(\text{C}_i\text{OH})} \times 100\%$$

$$s(\text{C}_i\text{H}_{jx}) = \frac{i \bullet n(\text{C}_i\text{H}_{jx})}{\sum i \bullet n(\text{C}_i\text{H}_{jx}) + n(\text{C}_i\text{OH})} \times 100\%$$

where n(C_iH_{jx}) and n(C_iOH) are the moles of various hydrocarbons (C_iH_{jx}) and alcohols generated in CO₂ hydrogenation respectively. The catalytic results obtained at 24 h were used for comparison. The carbon molar balances in various tests were in 95–100%.

3. Results and discussion

3.1. Catalytic performance of K-CuZnAl/Zr-CuFe composite for CO₂ hydrogenation to C₂₊OH

Fig. 1 shows that neat K-CuZnAl produces large amounts of CO with selectivity as high as 90%, while methanol, as expected, is the dominant product in (hydrocarbons + alcohols) at 300 °C and 4.0 MPa. The

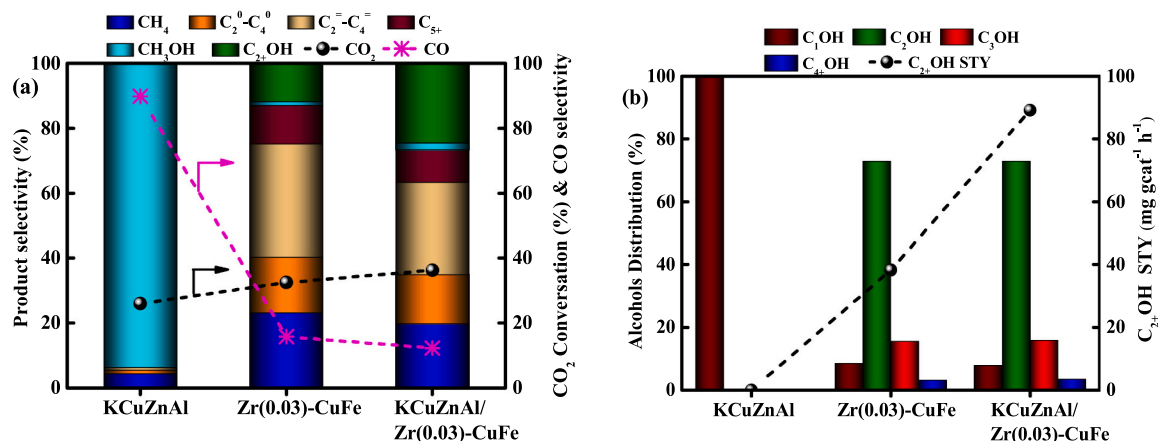


Fig. 1. Catalytic results of neat K-CuZnAl, neat Zr(0.03)-CuFe and K-CuZnAl/Zr(0.03)-CuFe composite in hydrogenation of CO₂ to C₂⁺OH at 300 °C, 4 MPa and GHSV of 6000 mL g_{cat}⁻¹ h⁻¹.

C₂⁺OH is undetectable, confirming that C-C coupling is negligible over the K-CuZnAl. On the neat Zr-CuFe, although certain amounts of C₂⁺OH are produced, the selectivity and STY of higher alcohols (C₂⁺OH) are only 11.9% and 38.2 mg g_{cat}⁻¹ h⁻¹ at the same reaction conditions. Interestingly, upon coupling of the K-CuZnAl and the Zr-CuFe catalysts, the C₂⁺OH selectivity and STY are considerably elevated to 24.5% and 89.1 mg g_{cat}⁻¹ h⁻¹, accompanied with increase of CO₂ conversion from 32.5% on neat Zr-CuFe to 36.3% on K-CuZnAl/Zr-CuFe composite, while the CO selectivity is declined from 15.8% to 12.3%. Among them, ethanol accounts for ~80% of C₂⁺OH. Notably, K-CuZnAl/Zr(0.03)-CuFe shows higher C₂⁺OH selectivity and STY than CuZnAl/Zr(0.03)-CuFe (Fig. S1), as K-CuZnAl produces more CO by suppressing

undesirable over-hydrogenation reaction [29].

The catalytic performance of K-CuZnAl/Zr-CuFe composite is dependent on the integration manner and the relative amounts of K-CuZnAl and Zr-CuFe components. By the dual-bed filling of Zr-CuFe (down) and K-CuZnAl (upper), the CO₂ conversion and C₂⁺OH selectivity are only 31.1% and 18.0% respectively, along with CO selectivity of 17.0% (Fig. 2(a)), which corresponds a C₂⁺OH STY of 57.5 mg g_{cat}⁻¹ h⁻¹ (Fig. 2(b)). Decreases of the contact distance between the two components by granularly stacking (20 – 40 mesh) and by powder mixing increase CO₂ conversion and C₂⁺OH STY to 35.5% and 88.9 mg g_{cat}⁻¹ h⁻¹, and 36.3% and 89.1 mg g_{cat}⁻¹ h⁻¹, respectively (Fig. 2(b)). Simultaneously, the CO selectivity is lowered to 14.3% and 12.3%, respectively

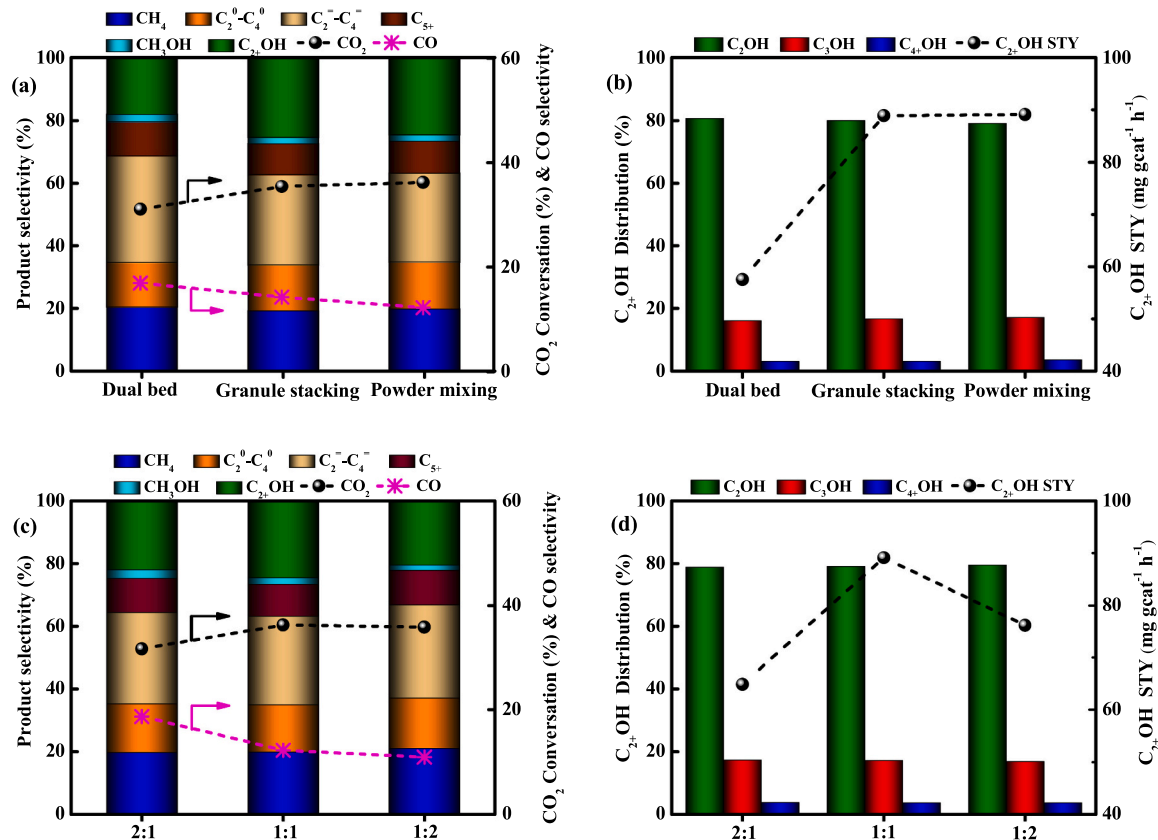


Fig. 2. Catalytic results of K-CuZnAl and Zr(0.03)-CuFe composites prepared by different integration manners (a and b), and K-CuZnAl and Zr(0.03)-CuFe composite by powder mixing different amounts of the two components (c and d) for CO₂ hydrogenation to C₂⁺OH at 300 °C, 4 MPa and GHSV of 6000 mL g_{cat}⁻¹ h⁻¹.

(Fig. 2(a)). This indicates that close contact of K-CuZnAl with Zr-CuFe favors the transformation of generated CO intermediates into higher alcohols. The optimal K-CuZnAl/Zr-CuFe mass ratio is 1/1. Introduction of more K-CuZnAl (K-CuZnAl/Zr-CuFe mass ratio of 2/1) produces more CO, which cannot be converted in time. However, when more Zr-CuFe (K-CuZnAl/Zr-CuFe mass ratio of 1/2) was added, large amounts of hydrocarbons were produced due to the promotion of CO dissociative activation (Figs. 2(c) and 2(d)).

Figs. 3(a) and 3(b) show that doping of Zr in CuFe has a vital role in the promotion of higher alcohols formation. K-CuZnAl/CuFe gave a C_{2+} OH selectivity of 20.5% and STY of $56.0 \text{ mg g}_{\text{cat}}^{-1} \text{ h}^{-1}$ with CO_2 conversion of 29.4% and CO selectivity of 21.0% at 300°C and 4.0 MPa. Introduction of small amounts of Zr in CuFe catalyst ($\text{Zr}(0.03)\text{-CuFe}$) significantly increases the CO_2 conversion and the C_{2+} OH selectivity to 36.3% and 24.5%, and decreases CO selectivity to 12.3%. This results in an elevation of C_{2+} OH STY from 56.0 to $89.1 \text{ mg g}_{\text{cat}}^{-1} \text{ h}^{-1}$, despite that a contrary result was obtained when further increasing Zr content.

The catalytic performance of K-CuZnAl/Zr(0.03)-CuFe composite is also related to the Cu/Fe ratio in Zr-CuFe catalyst (Figs. 3(c) and 3(d)), as it strongly influences dissociative and non-dissociative activation amounts of CO intermediate [31]. The CO selectivity is considerably decreased from 25.9% to 12.3%, along with the rise of CO_2 conversion and the C_{2+} OH STY from 28.2% and $58.4 \text{ mg g}_{\text{cat}}^{-1} \text{ h}^{-1}$ to 36.3% and $89.1 \text{ mg g}_{\text{cat}}^{-1} \text{ h}^{-1}$, when the Cu/Fe molar ratio is declined from 3/1 to 1/1. This indicates that enhancement of CO dissociative activation is beneficial to C_{2+} OH formation. Nevertheless, further increase of the Fe content (Cu/Fe molar ratio of 1/3) in Zr-CuFe results in the formation of more hydrocarbons due to serious CO over-dissociation.

The catalytic results of K-CuZnAl/Zr(0.03)-CuFe at different reaction temperature, pressure and space velocity are shown in Figs. S2-S4. Elevation of the reaction temperature raises the CO_2 conversion and lowers the CO selectivity (Fig. S2) [24]. The C_{2+} OH STY displays a

volcanic curve with the reaction temperature, and it reaches the maximum value of $93.3 \text{ mg g}_{\text{cat}}^{-1} \text{ h}^{-1}$ at 320°C . It has been shown that high temperature promotes the CO dissociative activation, but too high temperature significantly lowers non-dissociative CO contents, and thus reversely decreasing the selectivity and STY of higher alcohols but producing more hydrocarbons.

Increase of reaction pressure is, as expected, beneficial for improving the catalytic activity and higher alcohols selectivity. At 320°C , 4.0 MPa, $6000 \text{ mL g}_{\text{cat}}^{-1} \text{ h}^{-1}$ and H_2/CO_2 of 3/1, K-CuZnAl/Zr(0.03)-CuFe exhibits C_{2+} OH selectivity and STY of 22.4% and $93.3 \text{ mg g}_{\text{cat}}^{-1} \text{ h}^{-1}$, with CO_2 conversion of 40.6% and CO selectivity of 10.3% (Fig. S3). The C_{2+} OH STY is further improved by increasing space velocity. When the space velocity is increased to $24000 \text{ mL g}_{\text{cat}}^{-1} \text{ h}^{-1}$, the C_{2+} OH STY reaches $195.1 \text{ mg g}_{\text{cat}}^{-1} \text{ h}^{-1}$, although CO_2 conversion is reduced to 30% (Fig. S4). To the best of our knowledge, such a high STY of higher alcohols outperforms most of the iron-based samples in CO_2 hydrogenation to C_{2+} OH (Fig. 4 and Table S1).

The K-CuZnAl/Zr(0.03)-CuFe composite also exhibits long catalytic life in CO_2 hydrogenation. The C_{2+} OH selectivity and the STY on K-CuZnAl/Zr(0.03)-CuFe are still kept at around 20% and $180 \text{ mg g}_{\text{cat}}^{-1} \text{ h}^{-1}$, with CO_2 conversion of 26.0%, at 320°C , 4.0 MPa, $24000 \text{ mL g}_{\text{cat}}^{-1} \text{ h}^{-1}$ and H_2/CO_2 of 3/1 at least within 200 h (Fig. 5). Moreover, the ethanol in C_{2+} OH is also about ~80%. This shows that K-CuZnAl/Zr(0.03)-CuFe composite is an efficient catalyst for synthesis of higher alcohols from CO_2 hydrogenation.

3.2. Characterizations of K-CuZnAl/Zr-CuFe composite

XRD pattern of K-CuZnAl shows diffraction peaks of CuO at 2θ of 35.8° , 39.0° and 49.0° , and of ZnO at 2θ of 32.0° and 66.6° (Fig. S5(a)) [32]. No K-related species is detected, indicative of a high dispersion of K on CuZnAl, which is confirmed by its STEM-EDX elemental mapping

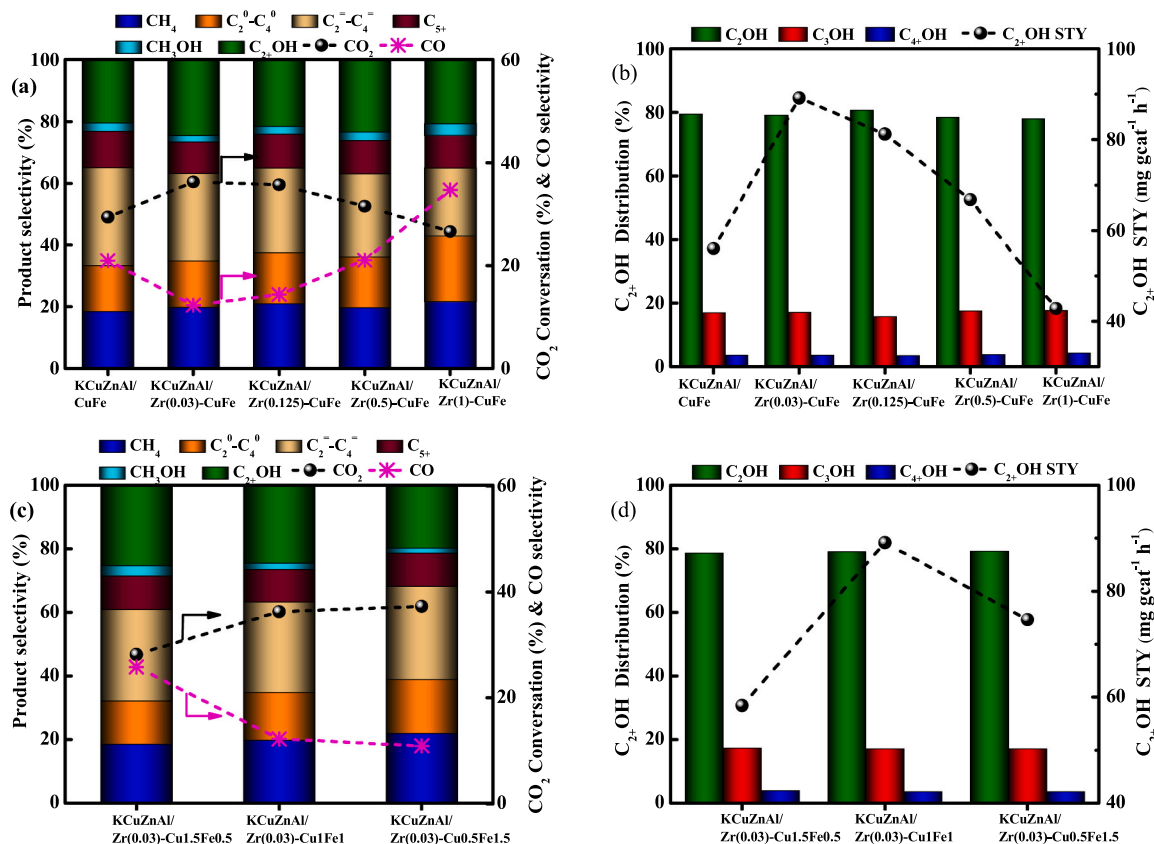


Fig. 3. Influences of Zr amount and Cu/Fe ratio in Zr-CuFe on the catalytic performance of K-CuZnAl/Zr-CuFe composite in CO_2 hydrogenation to C_{2+} OH at 300°C , 4 MPa and GHSV of $6000 \text{ mL g}_{\text{cat}}^{-1} \text{ h}^{-1}$.

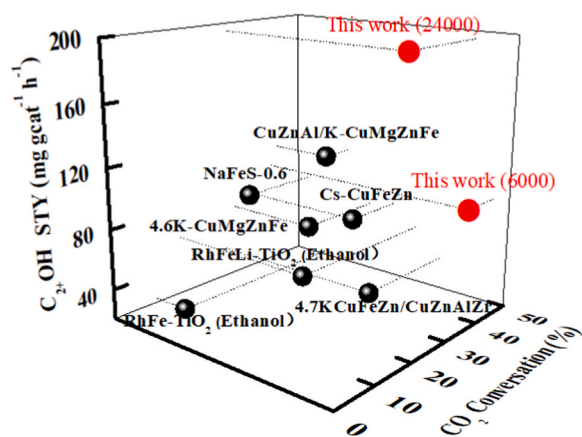


Fig. 4. The $C_{2+}OH$ STY obtained on K-CuZnAl/Zr(0.03)-CuFe composite and the reported Fe-based catalysts in literatures.

(Fig. S6). HRTEM images show only the lattice fringes of 0.252 nm and 0.232 nm, which are assigned to (1 1 -1) and (1 1 1) crystal facets of CuO (Figs. S5(c) and S5(d)). The N_2 sorption experiment reveals that the surface area and pore volume of K-CuZnAl are $48.5 \text{ m}^2 \text{ g}^{-1}$ and $0.256 \text{ cm}^3 \text{ g}^{-1}$ (Fig. S5(b)).

In the XRD patterns of CuFe catalysts, the peaks at 2θ of 35.8° , 39.1° and 48.9° , assigned to (1 1 -1), (1 1 1) and (2 0 -2) facets of CuO (JCPDS 96-900-8962), are obviously observed, while Fe species is difficult to be detected, indicating their low crystallinity (Fig. 6(a)). The HRTEM images also substantiate the presence of interplanar spacing

(0.238 nm) of CuO (Fig. 7(b)). The diffraction peaks of CuO slightly shifted to higher 2θ values when small amounts of Zr were introduced (Fig. 6(b)). This may be resulted from the incorporation of smaller Fe^{3+} ions (0.55 \AA) into the lattice of CuO (Cu^{2+} ionic radius of 0.73 \AA), which leads to a cell shrinkage. This is further verified by the HRTEM images and the Rietveld refinement results that the interplanar spacing and the cell volume of CuO in Zr(0.03)-CuFe are smaller than in CuFe (Fig. 7, Fig. S7 and Table S2). It is also corroborated by the Aberration-corrected high-resolution STEM (HR-STEM) images that Zr(0.03)-CuFe exhibits smaller lattice fringes of 0.236 nm (CuO(111)) and 0.255 nm (CuO (11-1)) than of CuFe (0.239 nm (CuO(111)) and 0.259 nm (CuO (11-1))) (Fig. S8).

The above results are consolidated by STEM images and EDX elemental mappings. Fig. 8(a) shows that the CuO and Fe_2O_3 components of CuFe catalyst are separately aggregated. Introduction of small amounts of Zr makes Cu and Fe elements become uniformly dispersed (Fig. 8(b)). In the H_2 -TPR profile of CuFe catalyst (Fig. 6(c)), the peaks in the range of $150\text{--}350^\circ\text{C}$ are due to CuO reduction to metallic Cu, whereas the broad one at above 400°C is ascribed to Fe_2O_3 reduction to Fe_3O_4 and further to metallic Fe [33]. Upon addition of small amounts of Zr, the reduction temperatures of both CuO and Fe_2O_3 (Zr(0.03)-CuFe) are elevated, indicative of a high dispersion of Cu and Fe species and the strong interaction between these two species. One might say that the reduction of Fe species should shift to lower temperature due to hydrogen spillover effect. However, introduction of small amounts of Zr seriously decreases the surface hydroxyl groups concentration of catalysts such as Zr(0.03)-CuFe (Table S3), which is unfavorable to the hydrogen spillover, thus leading to an elevation of Fe species reduction temperature. However, when more Zr is introduced in the CuFe catalysts, the reduction temperatures of CuO and Fe_2O_3 (Zr(1)-CuFe) shifts

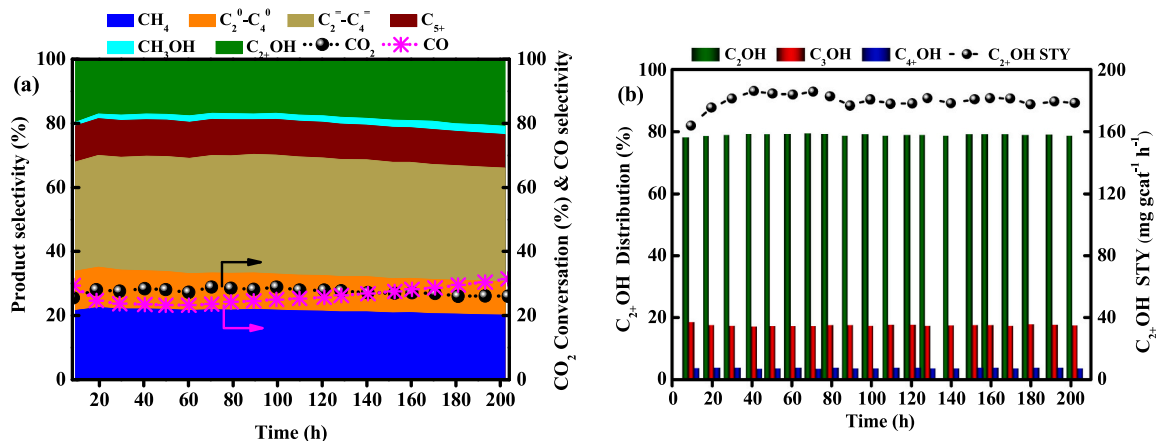


Fig. 5. Catalytic results of K-CuZnAl/Zr-CuFe composite within 200 h in CO_2 hydrogenation to $C_{2+}OH$ at 320°C , 4 MPa and GHSV of $24000 \text{ mL g}_{cat}^{-1} \text{ h}^{-1}$.

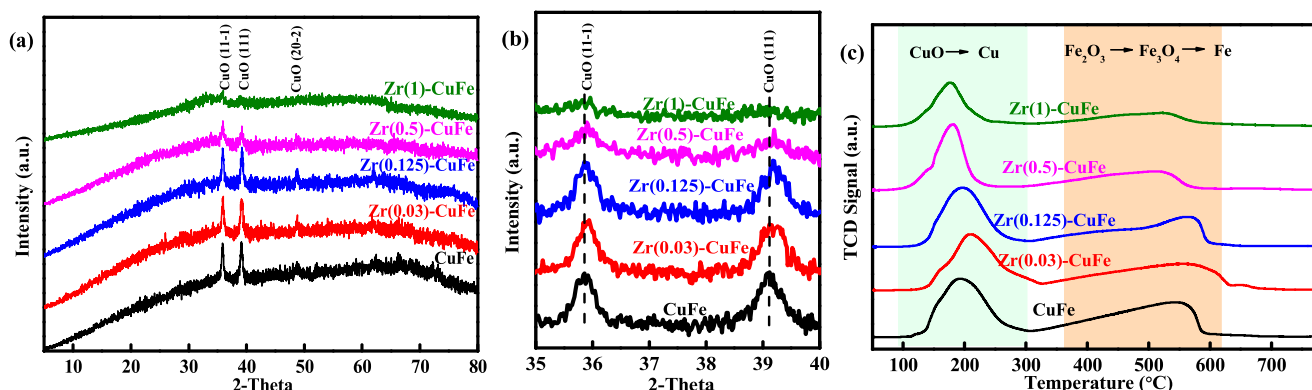


Fig. 6. XRD patterns in the 2θ region from 5 to 80° (a), and from 35 to 40° (b); and H_2 -TPR profiles (c) of Zr-CuFe catalysts with different Zr contents.

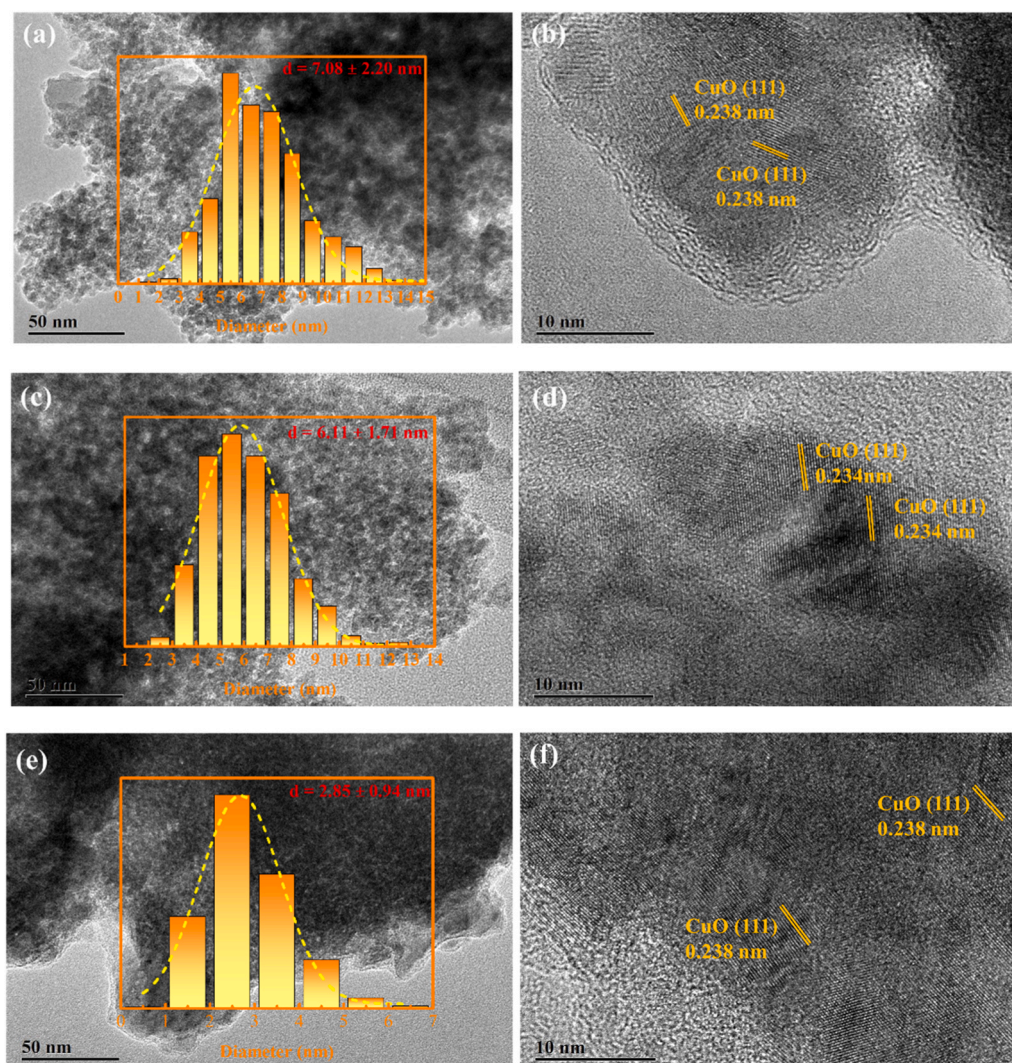


Fig. 7. TEM images and particle size distributions (a, c and e) and HRTEM images (b, d and f) of CuFe (a and b), Zr(0.03)-CuFe (c and d) and Zr(1.0)-CuFe (e and f) catalysts.

to lower temperature (Fig. 6(c)). The x-ray diffraction peak positions, the lattice fringes in HRTEM image and the cell volume obtained by Rietveld Refinement method of Zr(1)-CuFe are similar to those of CuFe catalyst (Figs. 6(b) and 7(f), Fig. S7 and Table S2). These characterization results indicate that excessive amounts of Zr is probably coated on the catalyst surface.

Fig. 7 shows that both CuFe and Zr-CuFe catalysts exhibit morphology of spherical nanoparticles with size ranging of around 2.8–7.1 nm. Introduction of Zr reduces the particle size, along with the increase of surface area, as a result of increase of Cu and Fe dispersions (Fig. 7, Fig. S9 and Table S2). Nevertheless, when large amounts of Zr is added in CuFeO_x, the intimacy between them is decreased although these two types of species are highly dispersed on ZrO₂ (ZrO₂ acts as support to anchor Cu and Fe species). This is revealed by the aberration-corrected HAADF-STEM images and EDX elemental mappings of Zr(1)-CuFe; the CuO and Fe₂O₃ are mostly separated (Fig. 8(c) and Fig. S10).

The interaction of Cu species with Fe is further investigated by XPS (Fig. 9). Doping small amounts of Zr shifts the binding energies of Fe(2p) to lower value, while moves the Cu(2p) XPS signals to higher value [34]. A deconvolution of in situ H₂ reduction Cu LMM Auger electron spectra by multi-peaks Gaussian fitting indicates that Zr(0.03)-CuFe has higher Cu⁺/Cu⁰ ratio than CuFe (Fig. S11). These results indicate a strong interaction between Cu and Fe species. The Bader charge calculation also reveals that the valence states of Cu atoms (0.145 |e|) are more

positive, whereas the Fe atoms at Cu-Fe interface are more negative charge (0.314 |e|) in Zr-CuFe than in CuFe catalyst (−0.004 |e| for Cu and 0.386 |e| for Fe) (Fig. S12). This verifies in theory that introduction of Zr facilitates the transfer of electrons from Cu to Fe, being consistent with XPS results (Figs. 9(a) and 9(b)). Notably, the variation of Cu and Fe XPS peak position between CuFe and Zr(0.125–1)-CuFe is not evident, suggesting that excessive amounts of Zr has insignificant effect on the electronic interaction of Cu and Fe. The Zr(3d) XPS of various samples show two intense peaks at around 181.9 and 184.3 eV, which are assigned to Zr 3d_{5/2} and Zr 3d_{3/2} of Zr⁴⁺ species respectively [35], indicating that the Zr species on Zr-CuFe samples mainly exist in the form of ZrO₂ (Fig. 9(c)).

The CO₂-TPD profiles show that CO₂ is more strongly adsorbed on Zr (0.03)-CuFe than on CuFe (Fig. 10(a)). Similar results were also obtained in CO-TPD (Fig. 10(b)). This is ascribed to the increase of the electron density around Fe sites (Fig. 9(a)) that promotes the back-donation of electrons to 2π* orbital of C–O bond of CO₂/CO [36,37]. It is consolidated by the charge difference density (CDD) calculation that CO has stronger electronic interaction with Zr-CuFe catalyst (Fig. S13), which results in an enhancement of CO adsorption energy from −0.04 eV on CuFe to −1.44 eV on Zr-CuFe (Fig. S14). As a result, K-CuZnAl/Zr (0.03)-CuFe gives higher CO₂ conversion (36.3%) and C₂+OH STY (89.1 mg g_{cat}^{−1} h^{−1}) but lower CO selectivity (12.3%) than K-CuZnAl/CuFe (CO₂ conversion of 29.4%, C₂+OH STY of 56.0 mg g_{cat}^{−1} h^{−1} and CO

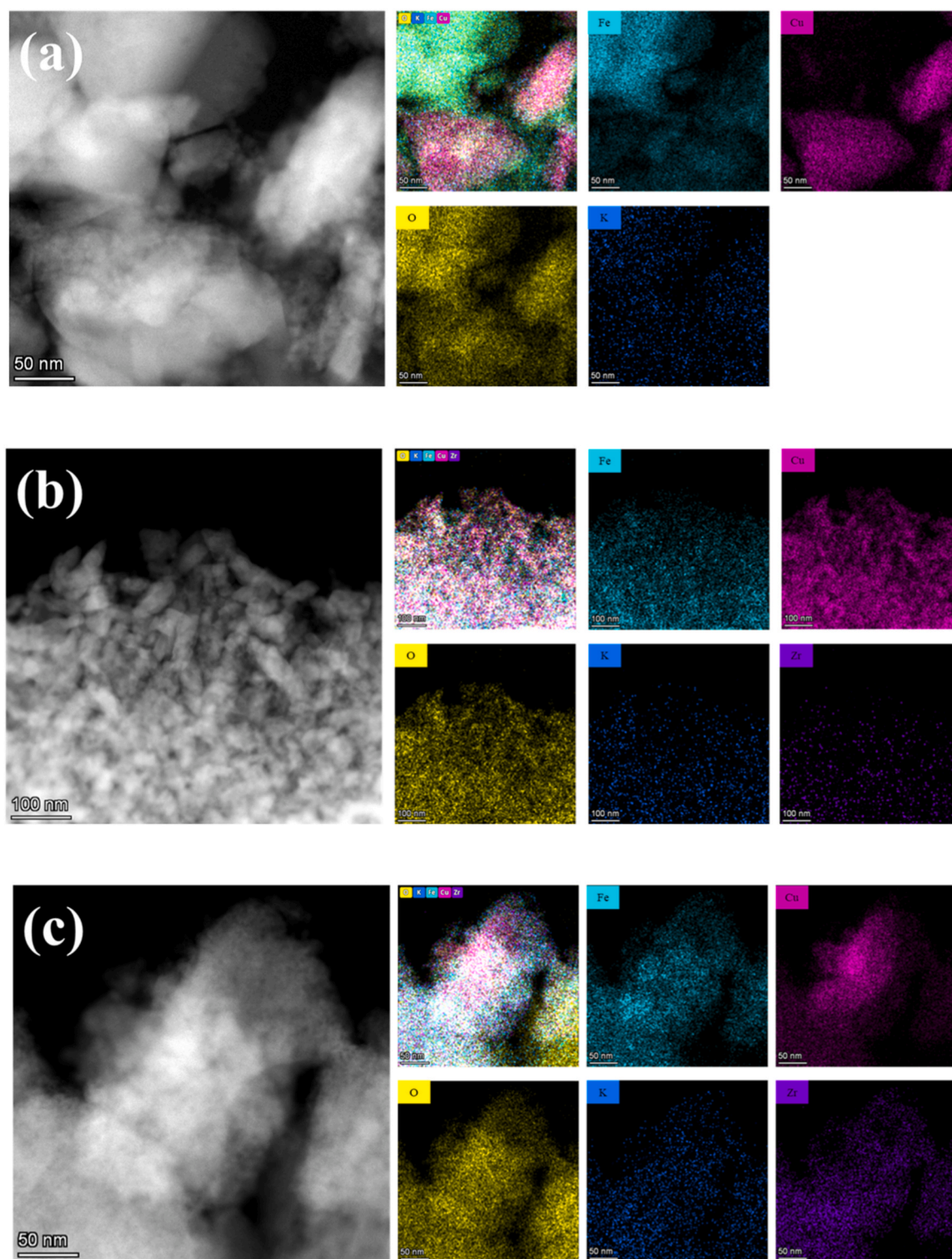


Fig. 8. Aberration-corrected HAADF-STEM images and EDX elemental mappings of CuFe (a), Zr(0.03)-CuFe (b) and Zr(1.0)-CuFe (c).

selectivity of 21%) at the same conditions (Figs. 3(a) and 3(b)). Notably, although the total adsorption amounts of CO_2 and CO on the samples increase with the Zr content, they are mainly contributed by the adsorption of CO_2 and CO at temperature $< 300^\circ\text{C}$. In the case of Zr (0.125–1)-CuFe with higher Zr contents, the desorbed amounts of CO_2/CO between 300 and 600°C are seriously decreased. Therefore, addition of excessive amounts of Zr cannot further improve CO_2 conversion and C_2+OH STY (Figs. 3(a) and 3(b)).

Fig. S15(a) shows that four types of oxygen species, viz. surface H_2O , surface hydroxyl groups, surface oxygen vacancies (O_v) and lattice oxygen atoms (O_L), are present in the samples. Introduction of Zr from 0 (CuFe) to 1.68 wt% (Zr(0.03)-CuFe) increases O_v concentration from 29.97% to 30.22%. Fig. S15(b) shows that Zr(0.03)-CuFe exhibits higher CO_2 conversion and C_2+OH STY but lower CO selectivity. However, when more Zr was added in the sample, it is mainly attached on the surface of CuFe, but not highly dispersed in the structure, consequently

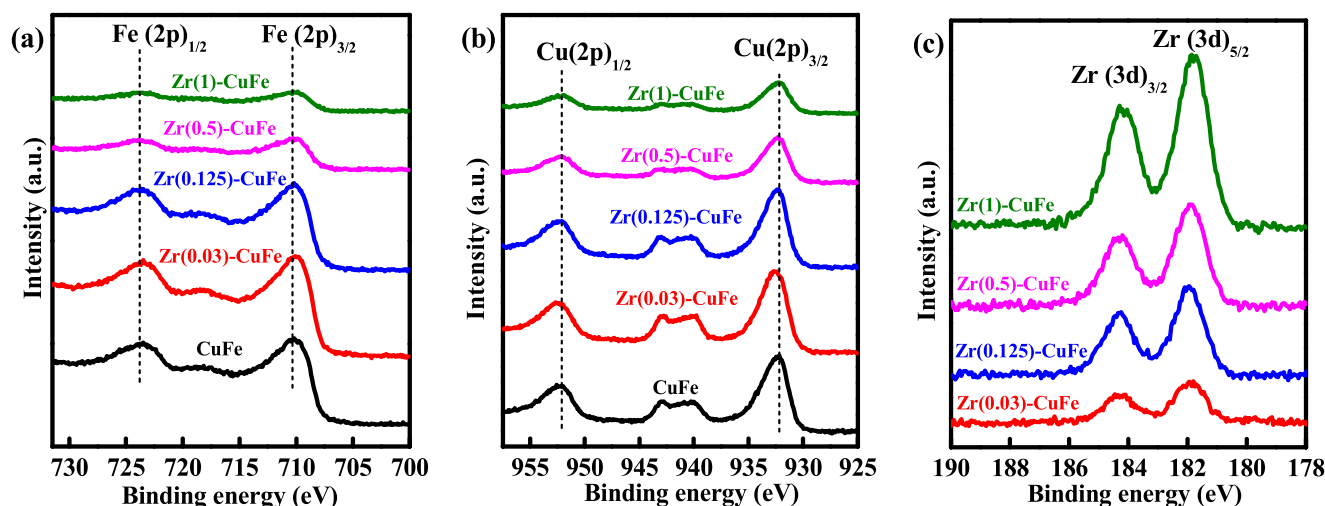


Fig. 9. Fe(2p) (a), Cu(2p) (b) and Zr(3d) XPS (c) of Zr-CuFe catalysts with different Zr contents.

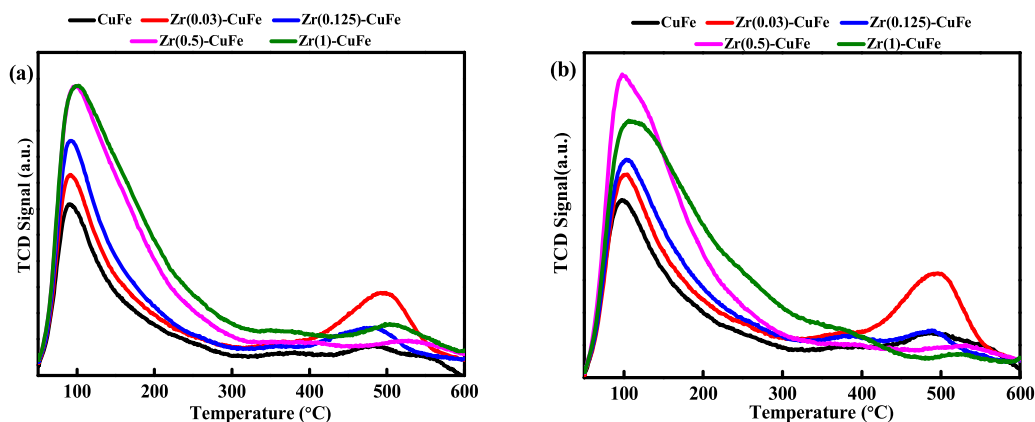


Fig. 10. CO₂-TPD (a) and CO-TPD (b) profiles of CuFe and various Zr-CuFe catalysts.

decreasing sites strongly adsorbing CO₂ and weakening CO₂ activation amounts, as indicated by the above CO₂-TPD results (Fig. 10(a)). Thus, although more surface oxygen vacancies were generated probably from attached amorphous ZrO₂, but they cannot improve but lower the catalytic performance of Zr-CuFe.

After reactions, the structure and electronic properties of used K-CuZnAl/Zr-CuFe and K-CuZnAl/CuFe samples were further analyzed. In the XRD patterns, the peaks at 2θ of 43.3°, 50.4° and 74.0° are ascribed to metallic Cu species (JCPDS 96-710-1265), whereas those at 31.7°, 34.4°, 56.5° and 62.8° are assigned to ZnO (JCPDS 96-900-4182) (Fig. 11(a)) [38]. In addition, some Hagg iron carbide (χ-Fe₅C₂) species are resolved at around 44.2° and 47.3° (JCPDS 01-089-7272) [39]. The presence of Fe₅C₂ on spent K-CuZnAl/Zr-CuFe and K-CuZnAl/CuFe catalysts is substantiated by ⁵⁷Fe Mössbauer spectra (Fig. 11(d) and Table S4). The structural information of spent samples is also analyzed by X-ray absorption near edge structure (XANES) and extended X-ray absorption fine structure spectroscopy (EXAFS). The Fe K-edge XANES spectra of spent K-CuZnAl/Zr-CuFe and K-CuZnAl/CuFe are different from those of standard Fe₃O₄, Fe₂O₃, FeO and Fe-foil samples due to formation of FeC_x species [40]. This is corroborated by the result that two evident peaks at around 1.6 and 2.1 Å, attributed to the Fe-C and Fe-Fe scatterings of Fe₅C₂ species [41], are detected in Fe K-edge EXAFS spectra (Figs. 11(e) and 11(f)). Unobserving of the interplanar spacings of Fe-related species in the HRTEM images is probably due to their low crystallinity (Fig. S16). After reaction, the Cu and Fe species in spent K-CuZnAl/CuFe show large particles (Fig. 12(a)), whereas they are still

highly dispersed within used K-CuZnAl/Zr(0.03)-CuFe catalyst (Fig. 12 (b)). This gives another piece of evidence for the enhancement of interaction of Cu with Fe by Zr component. It is corroborated by the XPS results that Fe(2p) signals shift to lower value, but Cu(2p) slightly move to high value, which indicates an electron transfer from copper to iron (Figs. 11(b) and 11(c)). Cu LMM Auger electron reveals that K-CuZnAl/Zr(0.03)-CuFe contains more Cu⁺, but less Cu⁰ than K-CuZnAl/CuFe (Fig. S17).

3.3. Catalytic mechanism of KCuZnAl/Zr-CuFe for CO₂ hydrogenation to higher alcohols

Compared with neat Zr-CuFe, K-CuZnAl/Zr-CuFe composite can effectively boost higher alcohols synthesis, as introduction of K-CuZnAl provides abundant CO intermediates in CO₂ hydrogenation that promote the reaction of CO and CH_x [28,31]. This is supported by the result that co-feeding small amounts of CO significantly improves the C₂+OH STY on neat Zr-CuFe catalyst in CO₂ hydrogenation (Fig. S18). Notably, the C₂+OH STY shows a volcanic curve with the co-fed CO content, as introduction of excessive amounts of CO cannot be converted in time (Fig. S19). In addition, the desorption energy of CO* is more negative on K-CuZnAl (−0.41 and −0.46 eV at 300 and 325 °C) than on Zr-CuFe (0.47 and 0.42 eV at 300 and 325 °C) (Fig. 13). This suggests that the generated CO* will quickly desorb from K-CuZnAl. Therefore, decrease of the contact distance of the two components is conducive to the rapid migration of CO* from K-CuZnAl to Zr-CuFe, and further the reaction

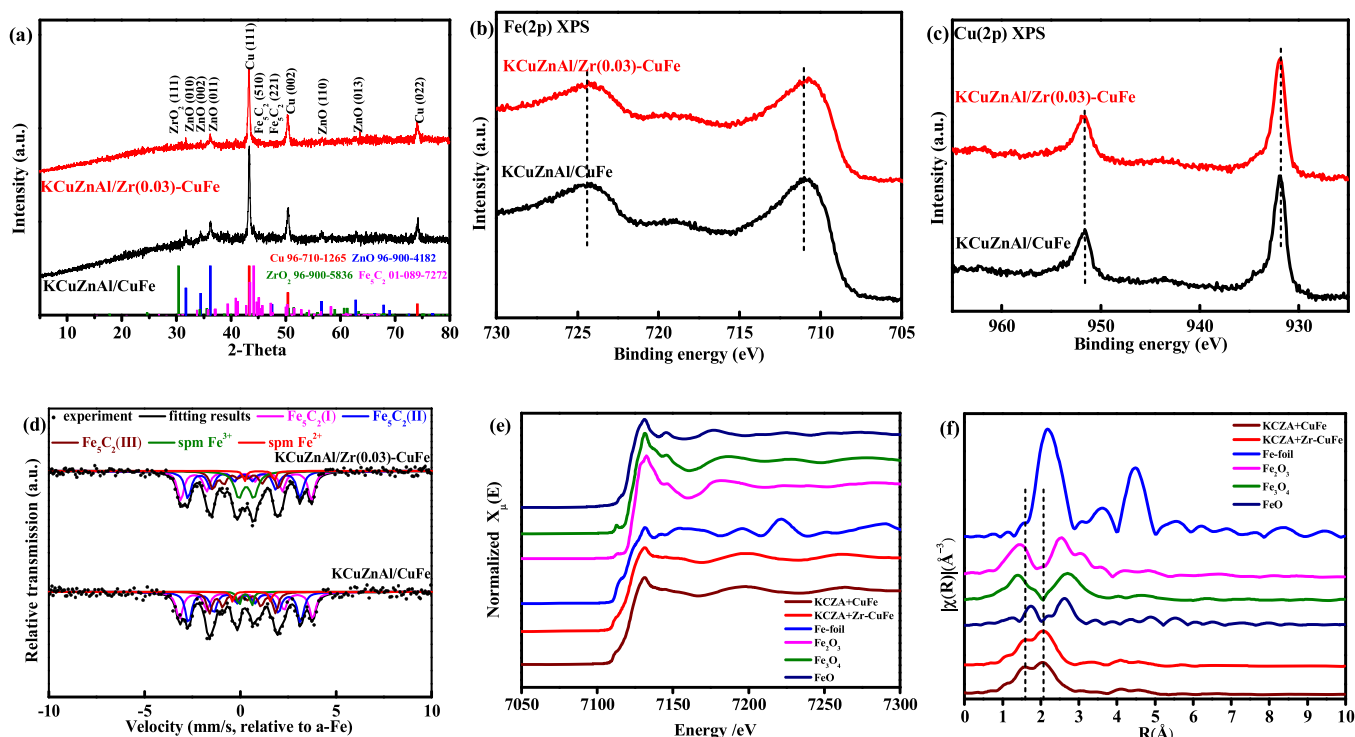


Fig. 11. XRD patterns (a), Fe(2p) XPS (b) and Cu(2p) XPS (c), ⁵⁷Fe Mössbauer spectra (d), and Fe XANES (e) and EXAFS (f) of used K-CuZnAl/CuFe and K-CuZnAl/Zr(0.03)-CuFe.

with CH_x* species (Fig. 2).

The catalytic mechanisms of K-CuZnAl/CuFe and K-CuZnAl/Zr-CuFe in CO₂ hydrogenation are further investigated by temperature- and time-dependent in situ DRIFTS. K-CuZnAl/CuFe was firstly reduced at 400 °C for 60 min, followed by cooling to 100 °C. Then, the H₂ and CO₂ gaseous mixture was fed into the reaction cell. When the temperature was lifted to 140 °C, some characteristic peaks appeared at ~1606, 1546 and 1332 cm⁻¹. These vibration peaks are ascribed to carboxylate and formate species, and intensified with the reaction temperature (Fig. 14 (a)) [42]. At 160 °C, the peak at 1066 cm⁻¹, characteristic of methoxy species, was observed [43]. Further elevation of temperature to 300 °C resulted in the formation of CO* (2177 and 2115 cm⁻¹) [44,45]. The CO* species was subsequently converted into CH_x* species through C-O dissociation and hydrogenation, as confirmed by the observation of C-H symmetric and asymmetric stretching vibration peaks of CH_x* species at 1400–1480 cm⁻¹ [46]. Interestingly, the peaks associated with acetate (1681 cm⁻¹) and acetaldehyde (1747 and 1735 cm⁻¹) were also detected over K-CuZnAl/CuFe [47,48].

In comparison, introduction of Zr made the formation of carboxylate and formate species more easily. The peaks characteristic of carboxylate and formate species (at 1612 cm⁻¹, 1556 cm⁻¹ and 1390 cm⁻¹) were clearly observed at lower reaction temperature of 120 °C (Fig. 14(b)). The peaks, assigned to methoxy groups, were detected at 1054 and 1087 cm⁻¹ at 140 °C. When the temperature was raised to 280 °C, the peaks associated with CO* appeared, and gradually enhanced with the reaction temperature. In addition, despite that some CH_x* species (1400–1480 cm⁻¹) were also detected on K-CuZnAl/Zr(0.03)-CuFe, their content is much lower than that on K-CuZnAl/CuFe. More interestingly, the peaks of acetate (1691 and 1675 cm⁻¹) and acetaldehyde (1747, 1725 and 1573 cm⁻¹) in the spectrum of K-CuZnAl/Zr-CuFe is more intense than in the spectrum of K-CuZnAl/CuFe, confirming that doping small amounts of Zr into CuFe catalyst can effectively promote acetate and acetaldehyde intermediates formation in CO₂ hydrogenation.

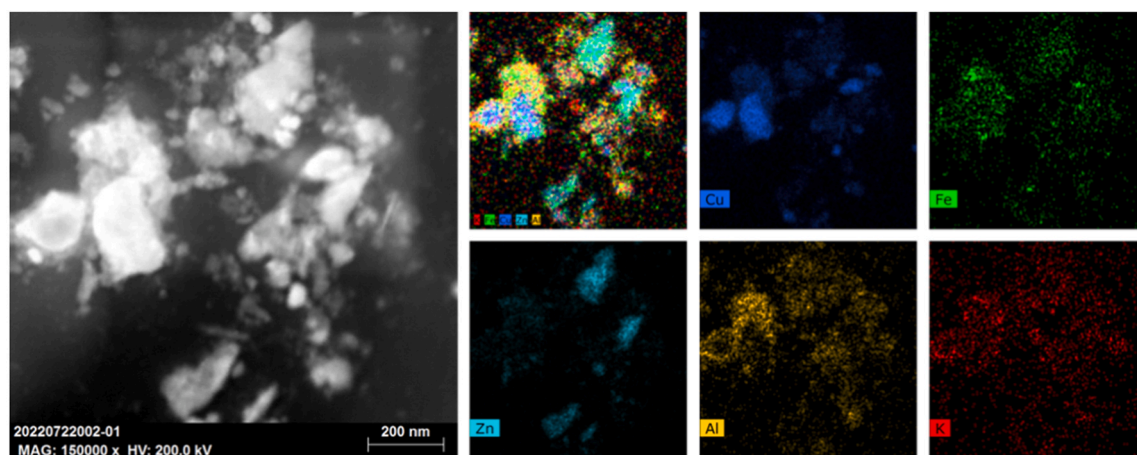
Fig. 14(c) and (d) display the time-dependent in situ DRIFTS of

steady CO₂ hydrogenation at 300 °C. After reaction of 2.5 min, the peaks of carboxylate and formate species were detectable at 1606, 1552 and 1346 cm⁻¹ and promptly intensified with the reaction time on both K-CuZnAl/CuFe and K-CuZnAl/Zr-CuFe. At 5 min, the peak of methoxy groups is identified at 1066 cm⁻¹ [49]. As expected, the peaks at 1697 and 1685 cm⁻¹, and at 1751 and 1737 cm⁻¹ assigned to the acetate and acetaldehyde intermediates, respectively, were also clearly observed at about 10 min on K-CuZnAl/Zr-CuFe, but these peaks were nearly undetectable even after 30 min on K-CuZnAl/CuFe.

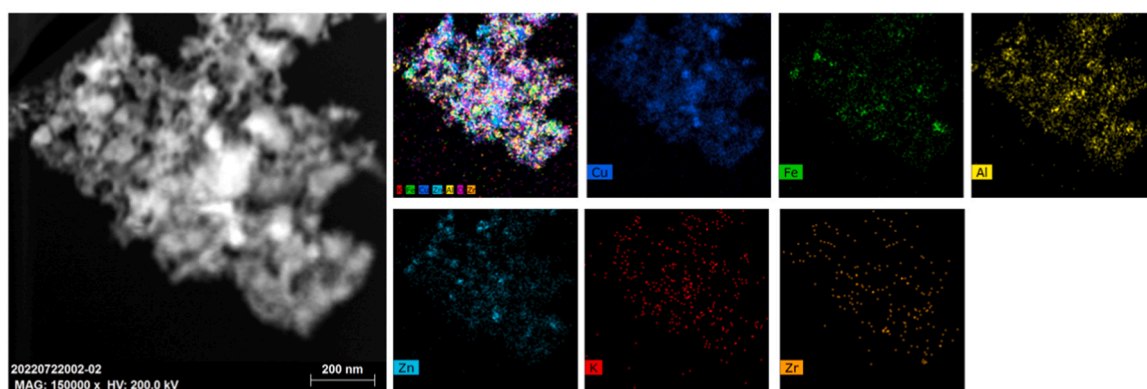
Since CO plays a vital role in CO₂ hydrogenation to C₂+OH. The reaction mechanisms of CO hydrogenation over CuFe and Zr(0.03)-CuFe were also investigated by in situ DRIFTS (Figs. 15(a) and 15(b)). At 300 °C, the two intense peaks of acetate and acetaldehyde species were detected on Zr(0.03)-CuFe, and gradually enhanced with the reaction time. In contrast, although these characteristic peaks were also visible on CuFe, their intensity was seriously lower, while the C-H symmetric and asymmetric stretching vibration peaks of CH_x* species (at 1400–1480 cm⁻¹) were more intense, indicating formation of more CH_x* species.

Fig. 15(c) and (d) shows the temperature-programmed surface reaction (CO-TPSR) profiles recorded by PTR TOF MS on the CuFe and Zr(0.03)-CuFe in CO hydrogenation. The onset temperature for the formation of acetate intermediates over the Zr(0.03)-CuFe is around 290 °C, being lower than that over the CuFe (310 °C). The signal of acetate is quickly intensified with the increase of reaction temperature up to 375 °C, and then attenuated due to its further transformation. Nevertheless, Zr(0.03)-CuFe produces more acetate intermediates than CuFe regardless of the reaction temperature and time, as substantiated by the result obtained in the steady CO hydrogenation at 300 °C.

The above results indicate that introduction of K-CuZnAl enhances the RWGS reaction and produces more CO* intermediates. These CO* species quickly diffuse onto the Zr-CuFe catalyst and promote the formation of more higher alcohols via CO* insertion reaction. Therefore, K-CuZnAl/Zr-CuFe composite shows higher CO₂ conversion and C₂+OH selectivity and STY than neat Zr-CuFe at the same conditions (Fig. 1).



(a)



(b)

Fig. 12. STEM images and EDX elemental mappings of spent K-CuZnAl/CuFe (a) and K-CuZnAl/Zr(0.03)-CuFe (b).

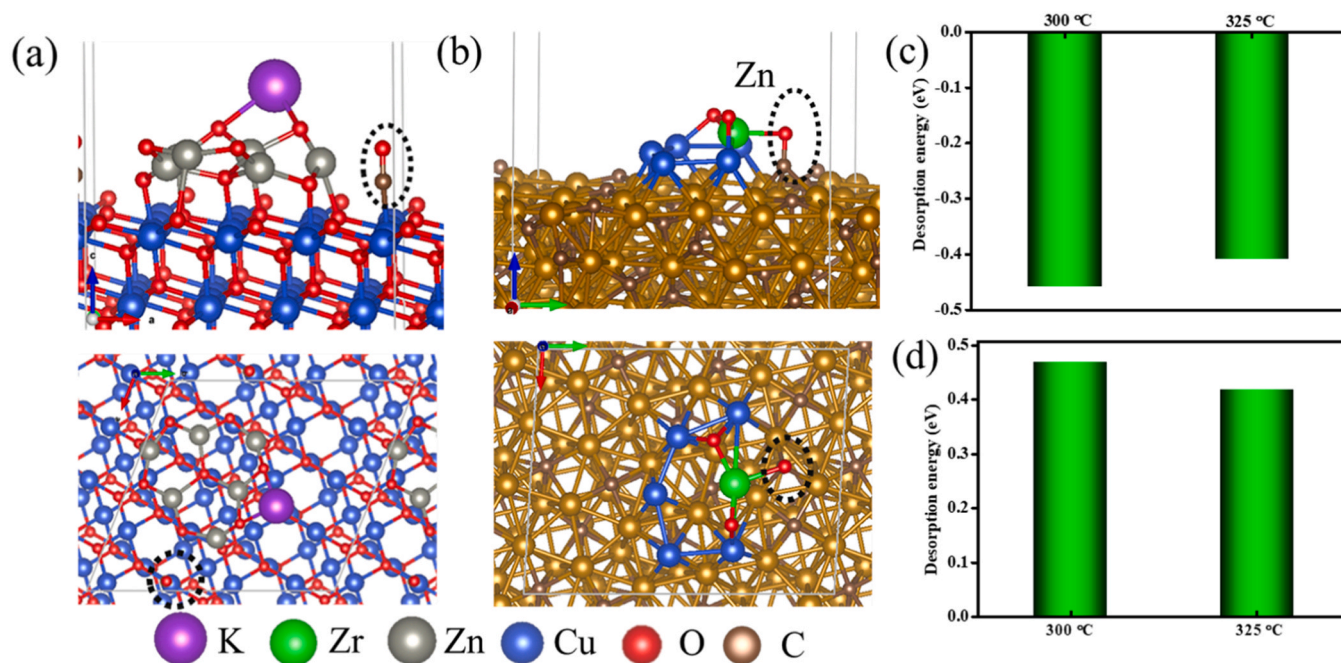


Fig. 13. Optimized structure of CO* adsorbed on the KCuZnAl (a) and Zr-CuFe (b), and the calculated CO* desorption energy on KCuZnAl (c) and Zr-CuFe (d).

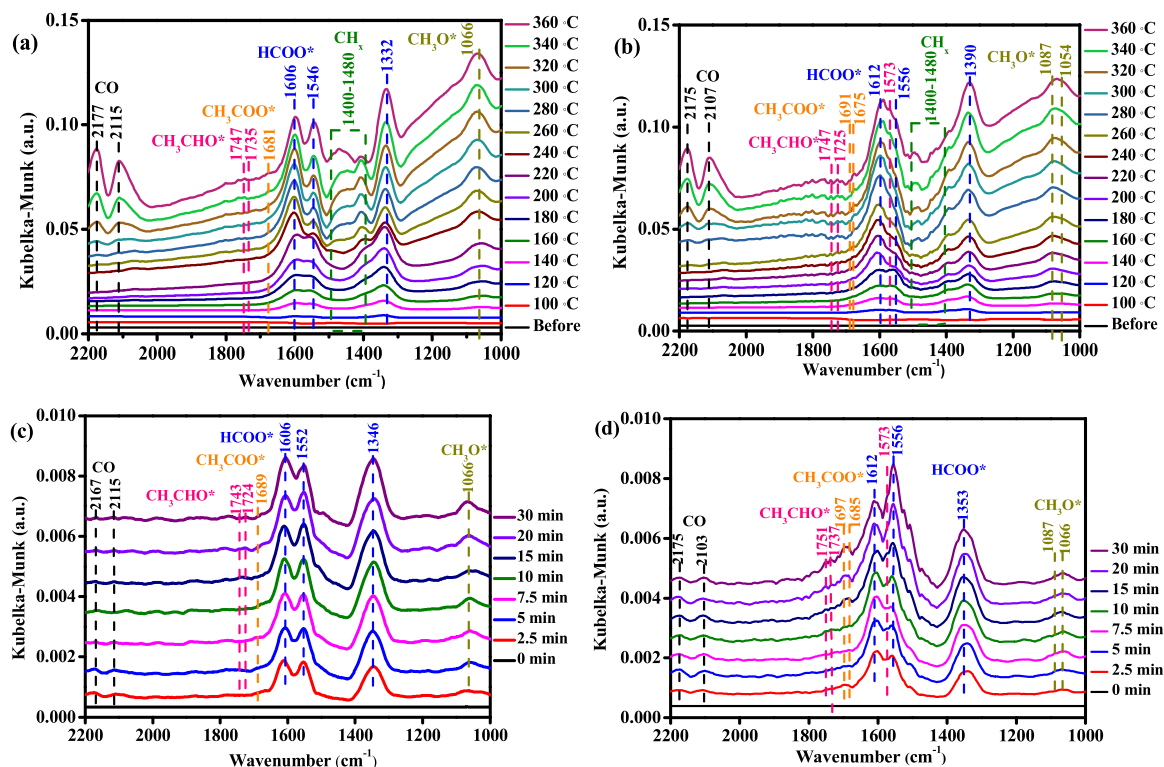


Fig. 14. Temperature-dependent (a and b) and time-dependent (c and d) in situ DRIFTS for hydrogenation of CO₂ on K-CuZnAl/CuFe (a and c) and K-CuZnAl/Zr(0.03)-CuFe (b and d).

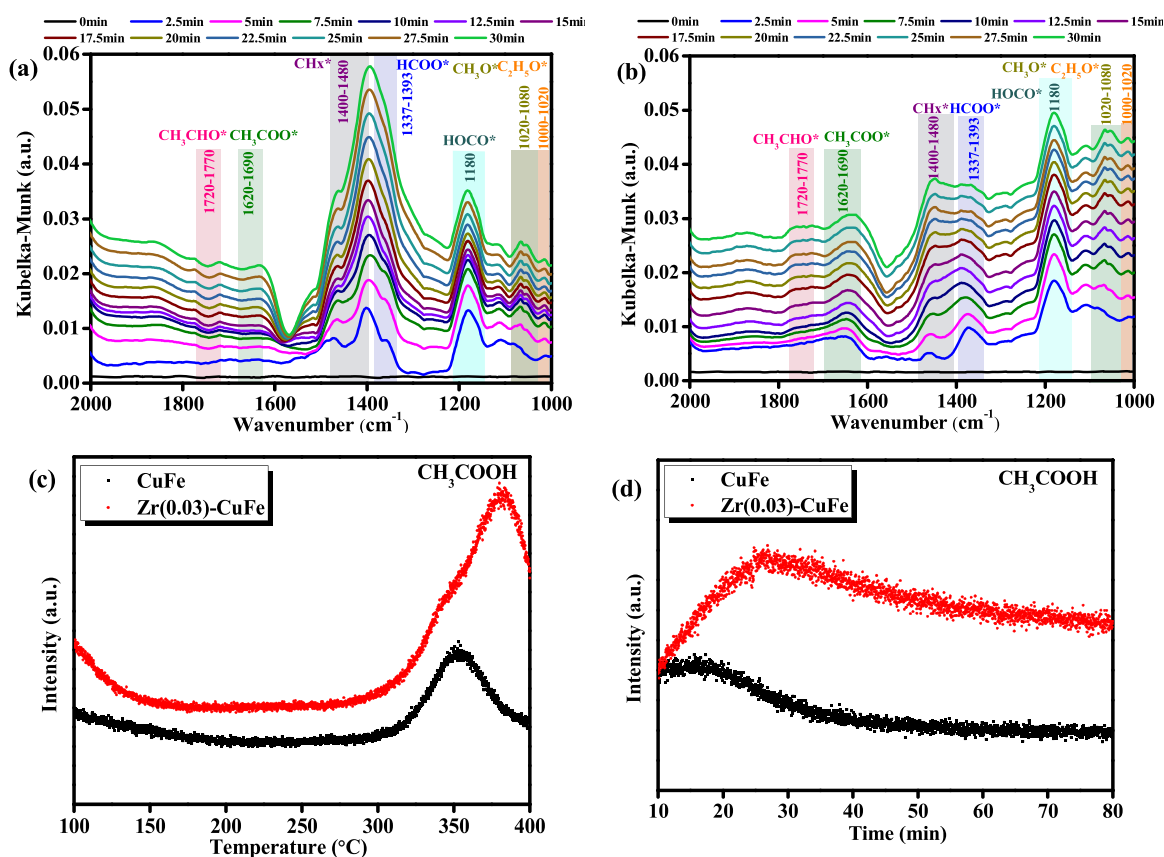


Fig. 15. In situ DRIFTS for CO hydrogenation on CuFe (a) and Zr(0.03)-CuFe (b) catalysts; TPSR profiles recorded by PTR TOF-MS on CuFe and Zr(0.03)-CuFe catalysts in CO hydrogenation at different temperature (c) and reaction time (d).

Besides increase of the CO* intermediate concentration, the balance between dissociative and non-dissociative activation of CO* is another key factor for higher alcohols production. Recent investigations propose that iron carbide (e.g. Fe₅C₂) is the main catalytic site for the formation of CH_x* species via CO dissociative activation [23–25]. These generated CH_x* species can be further converted into hydrocarbons through CH_x*–CH_x* coupling, or transformed into higher alcohols through interaction with non-dissociative adsorbed CO* [50]. Undoubtedly, the highly dispersed Fe and Cu species generally have strong interaction, which promotes the reaction of CO* with CH_x* to produce more higher alcohols. The Rietveld refined XRD, XPS, H₂-TPR, CO₂-TPD, CO-TPD, Aberration-corrected HAADF-STEM and EDX elemental mapping, in situ DRIFTS, PTR TOF-MS and DFT calculation results confirm that introduction of proper amounts of Zr into CuFe catalyst makes Cu and Fe species highly dispersed, and simultaneously induces electrons transferring from Cu to Fe, thus enhancing CO₂/CO adsorption and higher alcohols formation (Fig. 16 and Fig. S20). As a result, K-CuZnAl/Zr (0.03)-CuFe gave higher CO₂ conversion and C₂₊OH STY than K-CuZnAl/CuFe in CO₂ hydrogenation.

4. Conclusions

A new K-CuZnAl/Zr(0.03)-CuFe composite has been developed, and it shows outstanding performance in CO₂ hydrogenation to higher alcohols. The CO₂ conversion and the C₂₊OH selectivity reach 40.6% and 22.4% respectively, with CO selectivity of only 10.3%, at 320 °C, 4 MPa and space velocity of 6000 mL g_{cat}^{−1} h^{−1}. Increase of the space velocity to 24000 mL g_{cat}^{−1} h^{−1} elevates the C₂₊OH STY to 195.1 mg g_{cat}^{−1} h^{−1}, being higher than those of most of reported Fe-based catalysts. Such a high C₂₊OH STY is well maintained at least 200 h. It is confirmed that introduction of K-CuZnAl allows formation of more non-dissociative CO* species, and regulation of its proximity to Zr-CuFe promotes the reaction of CH_x species and CO*, which leads to generation of more higher alcohols. Doping small amounts of Zr into CuFe catalyst not only makes the Cu and Fe species highly dispersed, and hence, enhancing the interaction of Cu and Fe, but also facilitates the electrons transfer from Cu to Fe, which increases the electron density around Fe sites, and thus, leading to the back-donation of electrons to the 2π* orbital of C–O bond in CO₂/CO molecules. Therefore, the CH_x* species formed on iron carbide site to rapidly interact with the non-dissociative CO*, resulting in the production of much more C₂₊OH. This work reveals that a fine tuning of the Cu and Fe interface interaction is beneficial to preparing a highly efficient catalyst system for CO₂ hydrogenation to higher alcohols.

CRediT authorship contribution statement

Wang Jianguo: Conceptualization, Formal analysis, Investigation, Project administration. **Fan Weibin:** Conceptualization, Formal analysis, Funding acquisition, Investigation, Methodology, Project administration, Supervision, Writing – review & editing. **Dong Mei:** Conceptualization, Data curation, Funding acquisition, Investigation, Supervision. **Chen Jiangang:** Data curation, Formal analysis, Investigation. **Zhang Juan:** Data curation, Formal analysis, Investigation. **Zhang Qian:** Conceptualization, Data curation, Formal analysis, Investigation, Methodology, Validation, Writing – original draft. **Wang Sen:** Conceptualization, Formal analysis, Funding acquisition, Investigation, Project administration, Supervision, Writing – review & editing. **Shi Xuerong:** Formal analysis, Investigation, Methodology, Software.

Declaration of Competing Interest

The authors declare that they have no known competing financial interests or personal relationships that could have appeared to influence the work reported in this paper.

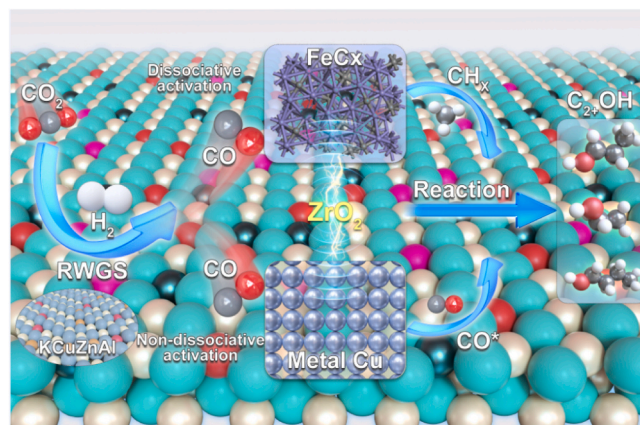


Fig. 16. Reaction scheme for hydrogenation of CO₂ to higher alcohols over K-CuZnAl/Zr-CuFe composite.

Data availability

Data will be made available on request.

Acknowledgements

This research was supported by the National Key Research and Development Program of China (2023YFB4103700), National Natural Science Foundation of China (U1910203; 21991090; 21991092; 22322208; 22272195; U22A20431), Natural Science Foundation of Shanxi Province of China (202203021224009), Innovation foundation of Institute of Coal Chemistry, Chinese Academy of Sciences (SCJC-DT-2023–06); Youth Innovation Promotion Association CAS (2021172); the foundation of National Key Laboratory of High Efficiency and Low Carbon Utilization of Coal (J23-24-603). The authors also sincerely thank Beijing Synchrotron Radiation Facility (BSRF) beamline for XANEX/EXAFS measurement.

Appendix A. Supporting information

Supplementary data associated with this article can be found in the online version at doi:10.1016/j.apcatb.2024.123748.

References

- [1] M.D. Porosoff, B. Yan, J.G. Chen, Catalytic reduction of CO₂ by H₂ for synthesis of CO, methanol and hydrocarbons: challenges and opportunities, *Energy Environ. Sci.* 9 (2016) 62–73.
- [2] A. Alvarez, A. Bansode, A. Urakawa, A.V. Bavykina, T.A. Wezendonk, M. Makkee, J. Gascon, F. Kapteijn, Challenges in the greener production of formates/formic acid, methanol, and DME by heterogeneously catalyzed CO₂ hydrogenation processes, *Chem. Rev.* 117 (2017) 9804–9838.
- [3] Y. Wang, L. Tan, M.H. Tan, P.P. Zhang, Y. Fang, Y. Yoneyama, G.H. Yang, N. Tsubaki, Rationally designing bifunctional catalysts as an efficient strategy to boost CO₂ hydrogenation producing value-added aromatics, *ACS Catal.* 9 (2019) 895–901.
- [4] J. Wei, Q.J. Ge, R.W. Yao, Z.Y. Wen, C.Y. Fang, L.S. Guo, H.Y. Xu, J. Sun, Directly converting CO₂ into a gasoline fuel, *Nat. Commun.* 8 (2017) 15174.
- [5] W. Zhou, K. Cheng, J.C. Kang, C. Zhou, V. Subramanian, Q.H. Zhang, Y. Wang, New horizon in C1 chemistry: breaking the selectivity limitation in transformation of syngas and hydrogenation of CO₂ into hydrocarbon chemicals and fuels, *Chem. Soc. Rev.* 48 (2019) 3193–3228.
- [6] P. Gao, S.S. Dang, S.G. Li, X.N. Bu, Z.Y. Liu, M.H. Qiu, C.G. Yang, H. Wang, L. S. Zhong, Y. Han, Q. Liu, W. Wei, Y.H. Sun, Direct production of lower olefins from CO₂ conversion via bifunctional catalysis, *ACS Catal.* 8 (2018) 571–578.
- [7] A. Ramirez, A. Dutta Chowdhury, A. Dokania, P. Cnudde, M. Caglayan, I. Yarulina, E. Abou-Hamad, L. Gevers, S. Ould-Chikh, K. De Wispelaere, V. Van Speybroeck, J. Gascon, Effect of zeolite topology and reactor configuration on the direct conversion of CO₂ to light olefins and aromatics, *ACS Catal.* 9 (2019) 6320–6334.
- [8] E.S. Gutterod, A. Lazzarini, T. Fjermestad, G. Kaur, M. Manzoli, S. Bordiga, S. Svelle, K.P. Lillerud, E. Skulason, S. Oien-Odegaard, A. Nova, U. Olsbye, Hydrogenation of CO₂ to methanol by Pt nanoparticles encapsulated in UiO-67: deciphering the role of the metal-organic framework, *J. Am. Chem. Soc.* 142 (2020) 999–1009.

- [9] S. Wang, L. Zhang, W. Zhang, P. Wang, Z. Qin, W. Yan, M. Dong, J. Li, J. Wang, L. He, U. Olsbye, W. Fan, Selective conversion of CO₂ into propene and butene, *Chem* 6 (2020) 3344–3363.
- [10] H. Luk, C. Mondelli, D. Ferre, J. Stewart, J. Perez-Ramirez, Status and prospects in higher alcohols synthesis from syngas, *Chem. Soc. Rev.* 46 (2017) 1358–1426.
- [11] M. Ao, G.H. Pham, J. Sunarso, M.O. Tade, S.M. Liu, Active centers of catalysis for higher alcohol synthesis from syngas: a review, *ACS Catal.* 8 (2018) 7025–7050.
- [12] J.W. Zhong, X.F. Yang, Z.L. Wu, B.L. Liang, Y.Q. Huang, T. Zhang, State of the art and perspectives in heterogeneous catalysis of CO₂ hydrogenation to methanol, *Chem. Soc. Rev.* 49 (2020) 1385–1413.
- [13] M.S. Frei, C. Mondelli, R. García-Muelas, K.S. Kley, B. Puertolas, N. Lopez, O. V. Safonova, J.A. Stewart, D. Curulla Ferre, J. Perez-Ramirez, Atomic-scale engineering of indium Oxide promotion by palladium for methanol production via CO₂ hydrogenation, *Nat. Commun.* 10 (2019) 3377.
- [14] J.J. Wang, G.N. Li, Z.L. Li, C.Z. Tang, Z.C. Feng, H.Y. An, H.L. Liu, T.F. Liu, C. Li, A highly active and stable ZnO-ZrO₂ solid solution catalyst for CO₂ hydrogenation to methanol, *Sci. Adv.* 3 (2017) e1701290.
- [15] J.T. Hu, L. Yu, J. Deng, Y. Wang, K. Cheng, C. Ma, Q.H. Zhang, W. Wen, S.S. Yu, Y. Pan, J.Z. Yang, H. Ma, F. Qi, Y.K. Wang, Y.P. Zheng, M.S. Chen, R. Huang, S. H. Zhang, Z.C. Zhao, J. Mao, X.Y. Meng, Q.Q. Ji, G.J. Hou, X.W. Han, X.H. Bao, Y. Wang, D.H. Deng, Sulfur vacancy-rich MoS₂ as a catalyst for the hydrogenation of CO₂ to methanol, *Nat. Catal.* 4 (2021) 242–250.
- [16] X.W. Nie, W.H. Li, X. Jiang, X.W. Guo, C.S. Song, Recent advances in catalytic CO₂ hydrogenation to alcohols and hydrocarbons, *Adv. Catal.* 65 (2020) 121–233.
- [17] Y. Lou, F. Jian, W. Zhu, L. Wang, T.Y. Yao, S.S. Wang, B. Yang, B. Yang, Y.F. Zhu, X. H. Liu, CeO₂ supported Pd dimers boosting CO₂ hydrogenation to ethanol, *Appl. Catal. B* 291 (2021) 120122.
- [18] S.X. Bai, Q. Shao, P.T. Wang, Q.G. Dai, X.Y. Wang, X.Q. Huang, Highly active and selective hydrogenation of CO₂ to ethanol by ordered Pd-Cu nanoparticles, *J. Am. Chem. Soc.* 139 (2017) 6827–6830.
- [19] J. Ke, Y.D. Wang, C.M. Wang, First-principles microkinetic simulations revealing the scaling relations and structure sensitivity of CO₂ hydrogenation to C₁ & C₂ oxygenates on Pd surfaces, *Catal. Sci. Technol.* 11 (2021) 4866–4881.
- [20] F.Y. Zhang, W. Zhou, X.W. Xiong, Y.H. Wang, K. Cheng, J.C. Kang, Q.H. Zhang, Y. Wang, Selective hydrogenation of CO₂ to ethanol over sodium-modified rhodium nanoparticles embedded in zeolite silicalite-1, *J. Phys. Chem. C* 125 (2021) 24429–24439.
- [21] Z.H. He, Q.L. Qian, J. Ma, Q.L. Meng, H.C. Zhou, J.L. Song, Z.M. Liu, B.X. Han, Water-enhanced synthesis of higher alcohols from CO₂ hydrogenation over a Pt/Co₃O₄ catalyst under milder conditions, *Angew. Chem. Int. Ed.* 55 (2016) 737–741.
- [22] X. Ye, C.Y. Yang, X.L. Pan, J.G. Ma, Y.R. Zhang, Y.J. Ren, X.Y. Liu, L. Li, Y. Q. Huang, Highly selective hydrogenation of CO₂ to ethanol via designed bifunctional Ir₁–In₂O₃ single-atom catalyst, *J. Am. Chem. Soc.* 142 (2020) 19001–19005.
- [23] G.B. Liu, G.H. Yang, X.B. Peng, J.H. Wu, N. Tsubaki, Recent advances in the routes and catalysts for ethanol synthesis from syngas, *Chem. Soc. Rev.* 51 (2022) 5606–5659.
- [24] D. Xu, M.Y. Ding, X.L. Hong, G.L. Liu, S.C.E. Tsang, Selective C₂₊ alcohol synthesis from direct CO₂ hydrogenation over a Cs-promoted Cu-Fe-Zn catalyst, *ACS Catal.* 10 (2020) 5250–5260.
- [25] D. Xu, M.Y. Ding, X.L. Hong, G.L. Liu, Mechanistic aspects of the role of K promotion on Cu–Fe-based catalysts for higher alcohol synthesis from CO₂ hydrogenation, *ACS Catal.* 10 (2020) 14516–14526.
- [26] F. Zeng, C. Mebrahtu, X.Y. Xi, L.F. Liao, J. Ren, J.X. Xie, H.J. Heeres, R. Palkovits, Catalysts design for higher alcohols synthesis by CO₂ hydrogenation: trends and future perspectives, *Appl. Catal. B* 291 (2021) 120073.
- [27] T.J. Lin, X.Z. Qi, X.X. Wang, L. Xia, C.Q. Wang, F. Yu, H. Wang, S.G. Li, L.S. Zhong, Y.H. Sun, Direct production of higher oxygenates by syngas conversion over a multifunctional catalyst, *Angew. Chem. Int. Ed.* 58 (2019) 4627–4631.
- [28] D. Xu, H.Q. Yang, X.L. Hong, G.L. Liu, S.C.E. Tsang, Tandem catalysis of direct CO₂ hydrogenation to higher alcohols, *ACS Catal.* 11 (2021) 8978–8984.
- [29] Y. Wang, K.Z. Wang, B.Z. Zhang, X.B. Peng, X.H. Gao, G.H. Yang, H. Hu, M.B. Wu, N. Tsubaki, Direct conversion of CO₂ to ethanol boosted by intimacy-sensitive multifunctional catalysts, *ACS Catal.* 11 (2021) 11742–11753.
- [30] D. Xu, M.Y. Ding, X.L. Hong, G.L. Liu, Mechanistic aspects of the role of K promotion on Cu–Fe-based catalysts for higher alcohol synthesis from CO₂ hydrogenation, *ACS Catal.* 10 (2020) 14516–14526.
- [31] Y.W. Li, W. Gao, M. Peng, J.B. Zhang, J.L. Sun, Y. Xu, S. Hong, X. Liu, X.W. Liu, M. Wei, B.S. Zhang, D. Ma, Interfacial Fe₃C₂-Cu catalysts toward low-pressure syngas conversion to long-chain alcohols, *Nat. Commun.* 11 (2020) 61.
- [32] E. Pahija, C. Panaritis, S. Gusarov, J. Shadabahr, F. Bensebaa, G. Patience, D. C. Boffito, Experimental and computational synergistic design of Cu and Fe catalysts for the reverse water-gas shift: a review, *ACS Catal.* 12 (2022) 6887–6905.
- [33] H.T. Luk, C. Mondelli, S. Mitchell, S. Siol, J.A. Stewart, D.C. Ferre, J. Perez-Ramirez, Role of carbonaceous supports and potassium promoter on higher alcohols synthesis over copper-iron catalysts, *ACS Catal.* 8 (2018) 9604–9618.
- [34] Y.W. Lu, R.G. Zhang, B.B. Cao, B.H. Ge, F.F. Tao, J.J. Shan, L. Nguyen, Z.H. Bao, T. P. Wu, J.W. Pote, B.J. Wang, F. Yu, Elucidating the copper-Hägg iron carbide synergistic interactions for selective CO hydrogenation to higher alcohols, *ACS Catal.* 7 (2017) 5500–5512.
- [35] S.S. Dang, P. Gao, Z.Y. Liu, X.Q. Chen, C.G. Yang, H. Wang, L.S. Zhong, S.G. Li, Y. H. Sun, Role of zirconium in direct CO₂ hydrogenation to lower olefins on oxide/zeolite bifunctional catalysts, *J. Catal.* 364 (2018) 382–393.
- [36] R.W. Yao, J. Wei, Q.J. Ge, J. Xu, Y. Han, Q.X. Ma, H.Y. Xu, J. Sun, Monometallic iron catalysts with synergistic Na and S for higher alcohols synthesis via CO₂ hydrogenation, *Appl. Catal. B* 298 (2021) 120556.
- [37] Y. Xu, P. Zhai, Y.C. Deng, J.L. Xie, X. Liu, S. Wang, D. Ma, Highly selective olefin production from CO₂ hydrogenation on iron catalysts: a subtle synergy between manganese and sodium additives, *Angew. Chem. Int. Ed.* 59 (2020) 21736–21744.
- [38] Z.L. Li, W.L. Wu, M.L. Wang, Y.N. Wang, X.L. Ma, L. Luo, Y. Chen, K.Y. Fan, Y. Pan, H.L. Li, J. Zeng, Ambient-pressure hydrogenation of CO₂ into long-chain olefins, *Nat. Commun.* 13 (2022) 2396.
- [39] J. Xu, J. Wei, J.X. Zhang, R.W. Yao, Q.J. Ge, Q.X. Ma, J. Sun, Highly selective production of long-chain aldehydes, ketones or alcohols via syngas at a mild condition, *Appl. Catal. B* 307 (2022) 121155.
- [40] K. Gong, Y. Wei, T.J. Lin, X.Z. Qi, F.F. Sun, Z. Jiang, L.S. Zhong, Maximizing the interface of dual active sites to enhance higher oxygenate synthesis from syngas with high activity, *ACS Catal.* 13 (2023) 4533–4543.
- [41] H.Y. Yang, Y.R. Dang, X. Cui, X.N. Bu, J. Li, S.G. Li, Y.H. Sun, P. Gao, Selective synthesis of olefins via CO₂ hydrogenation over transition-metal-doped iron-based catalysts, *Appl. Catal. B* 321 (2023) 122050.
- [42] S. Wang, L. Zhang, P.F. Wang, X.C. Liu, Y.Y. Chen, Z.F. Qin, M. Dong, J.G. Wang, L. He, U. Olsbye, W.B. Fan, Highly effective conversion of CO₂ into light olefins abundant in ethene, *Chem* 8 (2022) 1376–1394.
- [43] B.H. Yan, B.H. Zhao, S. Kattel, Q.Y. Wu, S.Y. Yao, D. Su, J.G.G. Chen, Tuning CO₂ hydrogenation selectivity via metal-oxide interfacial sites, *J. Catal.* 374 (2019) 60–71.
- [44] S.X. Lin, Q. Wang, M.S. Li, Z.W. Hao, Y.T. Pan, X.Y. Han, X. Chang, S.Y. Huang, Z. H. Li, X.B. Ma, Ni-Zn dual sites switch the CO₂ hydrogenation selectivity via tuning of the d-band center, *ACS Catal.* 12 (2022) 3346–3356.
- [45] X.J. Cui, S. Chen, H.H. Yang, Y.Q. Liu, H.F. Wang, H. Zhang, Y.F. Xue, G.F. Wang, L. Niu, T.S. Deng, W.B. Fan, Improving methanol selectivity in CO₂ hydrogenation by tuning the distance of Cu on catalyst, *Appl. Catal. B* 298 (2021) 120590.
- [46] Z.Y. Si, L.K. Wang, Y. Han, J.F. Yu, Q.J. Ge, C.Y. Zeng, J. Sun, Synthesis of Alkene and Ethanol in CO₂ Hydrogenation on a Highly Active Sputtering CuNaFe Catalyst, *ACS Sustain. Chem. Eng.* 10 (2022) 14972–14979.
- [47] L.X. Wang, S.X. He, L. Wang, Y. Lei, X.J. Meng, F.S. Xiao, Cobalt–nickel catalysts for selective hydrogenation of carbon dioxide into ethanol, *ACS Catal.* 9 (2019) 11335–11340.
- [48] L.X. Wang, L. Wang, J. Zhang, X.L. Liu, H. Wang, W. Zhang, Q. Yang, J.Y. Ma, X. Dong, S.J. Yoo, J.G. Kim, X.J. Meng, F.S. Xiao, Selective hydrogenation of CO₂ to ethanol over cobalt catalysts, *Angew. Chem. Int. Ed.* 57 (2018) 6104–6108.
- [49] S. Kattel, B. Yan, Y. Yang, J.G. Chen, P. Liu, Optimizing binding energies of key intermediates for CO₂ hydrogenation to methanol over oxide-supported copper, *J. Am. Chem. Soc.* 138 (2016) 12440–12450.
- [50] D. Xu, Y.Q. Wang, M.Y. Ding, X.L. Hong, G.L. Liu, S.C.E. Tsang, Advances in higher alcohol synthesis from CO₂ hydrogenation, *Chem* 7 (2021) 849–881.